JACS
JOURNAL OF THE AMERICAN CHEMICAL SOCIETY
pubs.acs.org/JACS
Article

Mechanistic Analysis of Metallaphotoredox C–N Coupling: Photocatalysis Initiates and Perpetuates Ni(I)/Ni(III) Coupling Activity

Nicholas A. Till, Lei Tian, Zhe Dong, Gregory D. Scholes, and David W. C. MacMillan*

Cite This: J. Am. Chem. Soc. 2020, 142, 15830–15841
Read Online

ABSTRACT: The combined use of reaction kinetic analysis, ultrafast spectroscopy, and stoichiometric organometallic studies has enabled the elucidation of the mechanistic underpinnings to a photocatalytic C–N cross-coupling reaction. Steady-state and ultrafast spectroscopic techniques were used to track the excited-state evolution of the employed iridium photocatalyst, determine the resting states of both iridium and nickel catalysts, and uncover the photochemical mechanism for reductive activation of the nickel cocatalyst. Stoichiometric organometallic studies along with a comprehensive kinetic study of the reaction, including rate–driving force analysis, unveiled the crucial role of photocatalysis in both initiating and sustaining a Ni(I)/Ni(III) cross-coupling mechanism. The insights gleaned from this study further enabled the discovery of a new photocatalyst providing a >30-fold rate increase.

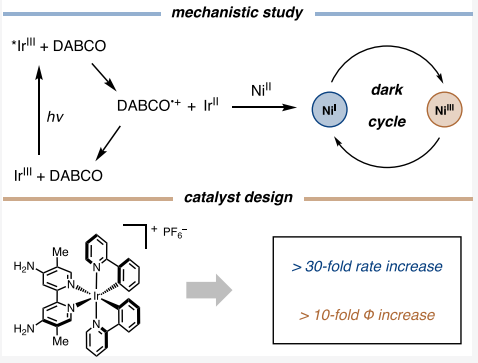

INTRODUCTION

Over the past 50 years, transition-metal-catalyzed cross-coupling reactions have risen to the forefront of synthetic technology, enabling rapid access to molecular complexity in medicinal chemistry, process chemistry, as well as materials science settings.[1−3] In order to promote a wide array of bond-forming processes through cross-coupling, the synthetic community has sought catalysts capable of undertaking a sequence of elementary organometallic steps in a generic and robust manner. To answer this call, major advances in Pd-catalyzed C–C and C–N cross-coupling technologies have resulted from the rational design of ligands.[4−6] Rates of oxidative addition,[7] transmetalation,[8] and reductive elimination[9] with a given transition-metal catalyst can all be tuned to achieve high reaction efficiencies through the judicious modulation of ligand electronic and steric properties. In particular, the ligand design work by Buchwald and Hartwig in the area of C–N cross-coupling stands as a quintessential example of this approach in the context of an especially important reaction to the practicing synthetic chemist. More specifically, tuning the steric and electronic parameters of mono- and bidentate phosphines[10−13] has enabled the often challenging C–N reductive elimination step, imparting the palladium-catalyzed arylation of amines with both high efficiency and broad scope.[14,15]

In recent years photocatalysis has emerged as a complementary alternative to ligand design, wherein visible light can "switch on" otherwise sluggish or inaccessible elementary organometallic steps such as transmetalation,[16] oxidative addition,[17] and reductive elimination.[18] The merger of transition-metal and photocatalysis has proven to be particularly advantageous in the context of facilitating challenging reductive elimination events to forge C–O,[18,19] C–N,[20] and C–CF_3[21,22] bonds, wherein photocatalysis provides access to high-valent or excited-state metal complexes (Ni(III), Ni(II)*, Cu(III), or Au(III)) poised for rapid bond formation. This reaction design principle was recently applied to the N-arylation of amines using a simple Ni(II) catalyst with no exogenous ligand and a mild organic base in combination with an Ir photocatalyst at a loading of 200 ppm to effect efficient and scalable C–N cross-coupling with a broad substrate scope.[23,24] In this way, the use of visible light photoactivation, rather than ligand design, appears to promote an otherwise challenging C–N bond formation. Given its synthetic relevance and operational simplicity, a detailed mechanistic description of this C–N cross-coupling would be valuable to both understanding and designing dual-catalytic systems (Figure 1). More broadly speaking, continued expansion of the repertoire of elementary organometallic steps available through visible light excitation requires a clear mechanistic understanding of the fundamental photochemical processes underlying the observed catalytic activity.

Received: May 30, 2020
Published: August 4, 2020

https://dx.doi.org/10.1021/jacs.0c05901
J. Am. Chem. Soc. 2020, 142, 15830–15841

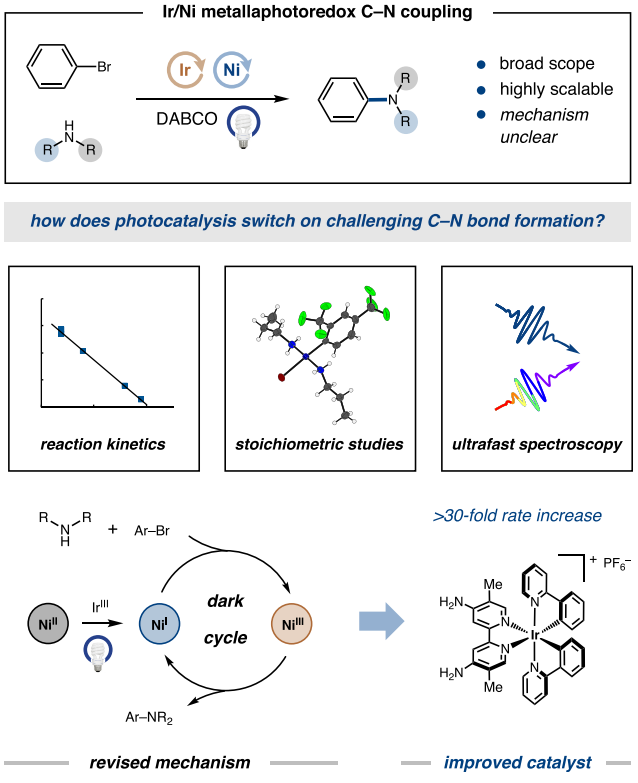

Figure 1. Mechanistic basis for C–N cross-coupling.

A key step in understanding photoinduced Ir/Ni-catalyzed cross-coupling pathways is determining the photochemical basis for Ni cocatalyst activation. Within the context of Ir(III) and Ru(II) photocatalysts typically employed in nickel/photoredox cross-coupling reactions, the long lifetimes (up to 2 μs), high triplet energies (often >2 eV), and high driving forces for reductive quenching ($E_{1/2}^{red}[M^{n}*/M^{n-1}]$ > +1 V vs SCE) of these photocatalysts' excited states allow for a multitude of diffusional quenching pathways.[25,26] In keeping with these photophysical characteristics, photoactivation of the nickel cocatalyst can take place through either energy transfer or electron transfer (ET), depending on the photophysical and electrochemical properties of the quenchers present in solution. In practice, both of these general quenching mechanisms have been observed: energy transfer to access a Ni(II)* excited state has been shown to promote C–O reductive elimination in a stoichiometric context[27] and initiate C–N bond formation in a related catalytic reaction reported by Miyake.[28] On the other hand, reductive quenching to access a high-valent Ni(III) intermediate is thought to enable C–O bond formation in the coupling of alcohols and aryl halides.[18,29]

While the primary photocatalyst quenching mechanism can be crucial in determining the mode of Ni catalysis, subsequent diffusional reactions can dramatically influence the eventual bond-forming process. As one example, recent work by Doyle has demonstrated that initially accessed Ni(II)* states can undergo subsequent electron transfer events to access Ni(III) and Ni(I) species.[30] In addition, Nocera and co-workers have shown that initial electron transfer quenching by an organic base indirectly facilitates formation of a Ni(III) complex capable of undergoing reductive elimination.[29] These considerations are particularly relevant to Ni-catalyzed C–X bond formation, wherein Ni(0)/Ni(II), Ni(I)/Ni(III), and Ni(0)/Ni(II)/Ni(III)/Ni(I) mechanisms have been variously proposed, and the relevance of these pathways may not be solely dependent on the initial photocatalyst quenching mechanism. Given these studies, we recognized that it would be necessary to not only determine the initial deexcitation mechanism for the photocatalyst but also further identify the ensuing energy or electron transfer pathways leading to the required C–N bond-forming step. For these reasons, a detailed mechanistic analysis involving kinetic, spectroscopic, and stoichiometric studies was undertaken to determine the specific roles of both iridium and nickel catalysts in this synthetically valuable C–N cross-coupling protocol. As a result, this in-depth study revealed that the Ni(0)/Ni(II)/Ni(III)/Ni(I) mechanism we originally proposed for the photoredox C–N cross-coupling is unlikely to be operative and instead supports a reassignment to a Ni(I)/Ni(III) pathway. This finding not only clarified the mechanistic understanding of the photoredox amination reaction but also provided crucial insight necessary for developing superior catalysts.

Photochemistry of the Iridium Catalyst. The aryl amination reaction shown in Table 1 requires both light and photocatalyst to achieve synthetically useful levels of C–N coupling (Table 1, entries 1–3). These control reactions make clear the crucial role of the photoexcited iridium catalyst in promoting this reaction. To initiate our study of the mechanism underlying the overall photocatalytic process, we first sought to determine the photochemical fate of the excited-state iridium catalyst under synthetically relevant reaction conditions. To this end, a comprehensive approach to establishing the major deexcitation pathway for the photocatalyst was taken. More specifically, all reaction components were evaluated as potential quenchers for the long-lived excited state (τ = 870 ns, Table S2, Figure S103) of photocatalyst **1** using steady-state emission measurements. A Stern–Volmer quenching analysis of photocatalyst **1** with DABCO, the soluble organic base employed in this reaction, revealed its high efficiency for quenching Ir(III)* photoluminescence (k_q = 2.75(0.07) × 10^9 M^{-1} s^{-1}, Figure 2A). Comparing this quenching efficiency with that of all remaining reaction components reveals the dominant role that DABCO plays in photocatalyst quenching ([DABCO] = 486 mM, Φ_q(DABCO) > 0.99, p S26). While these results clearly demonstrate that nearly every photon absorbed by the Ir(III) photocatalyst is

Table 1. Control Experiments for the C–N Coupling Reaction

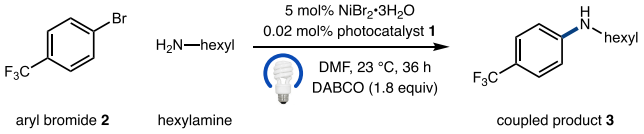

aryl bromide **2** hexylamine coupled product **3**

entry	conditions	yield[a]
1	no change	81%
2	no light	<1%
3	no **1**	<1%
4	no $NiBr_2·3H_2O$	<1%
5	no DABCO	14%

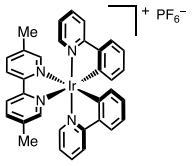

photocatalyst **1**

[a]Performed with 1.0 equiv of aryl bromide **2** and 1.5 equiv of hexylamine. Yields were determined by ^{19}F NMR analysis.

https://dx.doi.org/10.1021/jacs.0c05901
J. Am. Chem. Soc. 2020, 142, 15830–15841

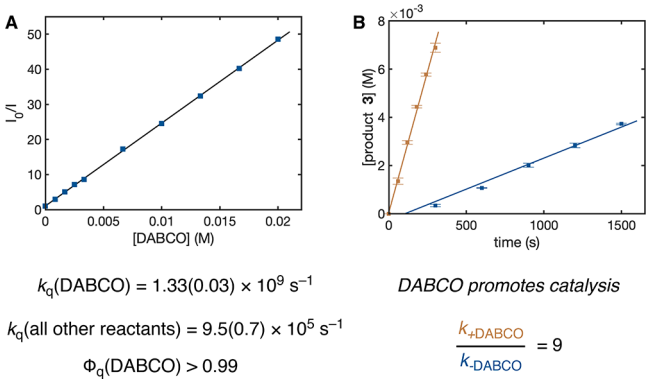

Figure 2. (A) Stern–Volmer luminescence quenching of **1** by DABCO. Standard error of the mean (n = 3) given in parentheses. (B) Initial rates of product formation in the C–N coupling reaction with (orange) and without DABCO (blue). Error bars represent the standard error of the mean (n = 2).

eventually funneled into this DABCO quenching pathway, it does not make clear that this quenching pathway is relevant to product formation. More specifically, this analysis leaves open the possibility of a low quantum yield process occurring rarely but nonetheless leading to the observed product-forming reactivity. To further interrogate the relevance of this dominant quenching pathway to product formation, initial rate measurements were carried out at various concentrations of DABCO. In the case that a low quantum yield quenching pathway is actually responsible for product formation, lower DABCO concentrations should increase the quantum yield of the product-forming pathway and thus the measured initial rate of product formation. Instead, the reaction rate decreases as a function of decreasing DABCO concentration (Figure S4), culminating in a full 9-fold decrease and significantly diminished final yield upon complete removal of DABCO from the reaction (Figure 2B and Table 1, entry 5), corroborating the relevance of DABCO quenching to the overall reactivity.

We next turned our attention to the mechanistic steps following the primary quenching process. Given the oxidizing power of the Ir(III)* excited state **4** ($E_{1/2}^{red}[Ir^{III}*/Ir^{II}]$ = +1.08 V vs SCE, Table S2) and relatively reducing nature of DABCO ($E_{1/2}^{red}[DABCO^{\bullet+}/DABCO]$ = +0.71 V vs SCE, Figure S65), we posited that DABCO quenching is reductive, giving rise to one-electron-reduced Ir(II) photocatalyst **5** and the one-electron-oxidized form of DABCO. The highly reducing and oxidizing natures of these two species ($E_{1/2}^{red}[Ir^{III}/Ir^{II}]$ = −1.41 V vs SCE, Figure S56, $E_{1/2}^{red}[DABCO^{\bullet+}/DABCO]$ = +0.71 V vs SCE, Figure S65) makes it possible that back electron transfer could rapidly follow the initial quenching electron transfer. This would return Ir(III) **1** in its ground-state form and neutral, closed-shell DABCO and potentially outcompete cage escape, thereby preventing any ensuing diffusional processes required for catalysis. In order to confirm

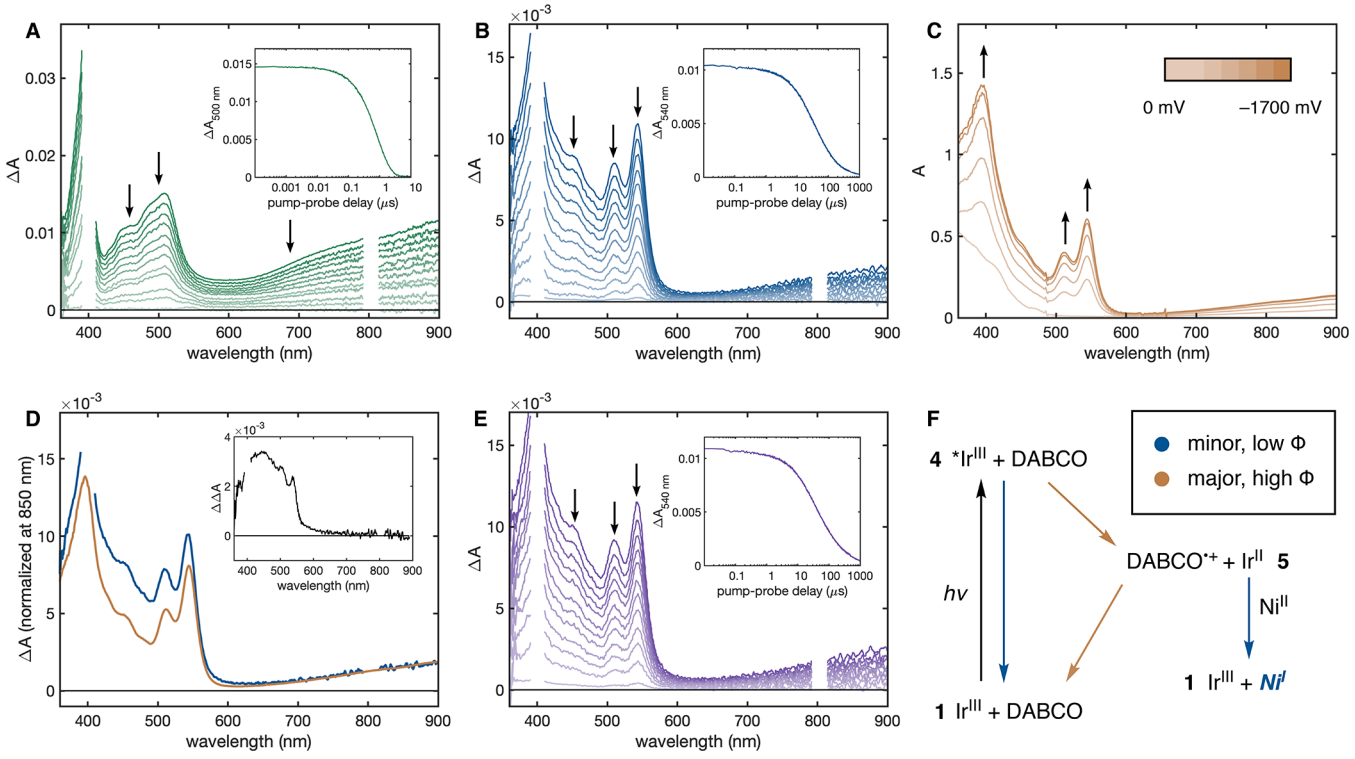

Figure 3. (A) Difference spectra at various pump–probe delays from a nanosecond to microsecond transient absorption measurement of **1** in DMF absent of quencher (λ_{pump} = 400 nm) and temporal evolution profile monitored at λ = 500 nm (inset). (B) Pump–probe difference spectra and temporal evolution profile monitored at λ = 540 nm (inset) for a mixture of **1** and DABCO (486 mM). (C) Absorption spectra of **1** in DMF at various applied voltages (from 0 to −1700 mV vs SCE). (D) Difference spectrum taken from B at 1000 ns pump–probe delay (blue), difference spectrum taken from C ($A(E$ = −1600 mV) − $A(E$ = 0 mV)) (orange) normalized at λ = 850 nm, and resulting difference spectrum from these two traces (blue–orange, inset). (E) Pump–probe difference spectra and temporal evolution profile monitored at λ = 540 nm (inset) for a mixture of **1**, DABCO (486 mM), aryl bromide **2** (270 mM), hexylamine (405 mM), and $NiBr_2 \cdot 3H_2O$ (13.5 mM). (F) Schematic representation of photochemical pathways for Ir(III) catalyst **1** and Ni(II) precatalyst.

https://dx.doi.org/10.1021/jacs.0c05901
J. Am. Chem. Soc. 2020, 142, 15830–15841

the presence of these proposed Ir(II) and DABCO radical cation electron transfer products as well as assess their temporal profiles, nanosecond−microsecond pump−probe spectroscopy was carried out alongside spectroelectrochemistry with iridium photocatalyst **1**. In a nanosecond pump−probe experiment with **1** in the absence of quencher, an excited-state absorption (ESA) feature forms within the rise time of the instrument and follows a monoexponential decay with a lifetime consistent with long-lived Ir(III)* **4** (τ = 850 ns), wherein recovery of the baseline occurs within 10 μs (Figure 3A). The excited-state dynamics of **1** in the presence of a catalytically relevant DABCO concentration (486 mM) differ markedly from the iridium-only dynamics. A positive feature distinct from the Ir(III)* ESA forms within the rise time of the instrument (consistent with the DABCO quenching rate determined by Stern−Volmer analysis) and exhibits distinct peaks at 510 and 540 nm (Figure 3B). This feature then decays on the late microsecond time scale, and a positive signal still persists on the early millisecond time scale ($[\Delta A_{540}(t = 1000\ \mu s)/\Delta A_{540}(t = 0)] = 2\%$) (Figure 3B, inset). Spectroelectrochemistry was performed on **1** to obtain an authentic Ir(II)/Ir(III) difference spectrum (Figure 3C). Increasingly negative applied potentials surpassing the reduction potential of **1** ($E_{1/2}^{red}[Ir^{III}/Ir^{II}] = -1.41$ V vs SCE, Figure S56) led to the growth of a positive feature with peaks centered at 510 and 540 nm. Comparison of the resulting Ir(II)/Ir(III) difference spectrum (obtained by subtracting the spectrum obtained at E = 0 mV from the E = −1600 mV spectrum) with the difference spectrum at an early pump−probe delay (t = 1000 ns) reveals broad agreement in peak shape and position, however, with a marked discrepancy in the 410−540 nm region (Figure 3D). In this wavelength region, significant positive signal in the pump−probe difference spectrum remains unaccounted for by the presence of Ir(II) **5** only. Subtracting the spectroelectrochemical data from the pump−probe data produces a broad positive peak centered around 460 nm, which matches well with previously reported visible absorption spectra for the DABCO radical cation (Figure 3D, inset).[31] Taken together, these data support the originally posited electron transfer products of the initial quenching event, namely, reduced state Ir(II) **5** and $DABCO^{\bullet+}$. Moreover, the long-lived nature of the signal demonstrates that a significant portion of the electron transfer products undergo solvent cage escape and are therefore capable of diffusional processes potentially necessary for facilitating C−N cross-coupling.

To confirm the presence of Ir(II) **5** and to probe its subsequent diffusional electron transfer pathways under the catalytically relevant reaction conditions, a second pump−probe experiment was carried out with photocatalyst **1**, DABCO (486 mM), and the remaining reaction components, namely, aryl bromide **2** (270 mM), hexylamine (405 mM), and $NiBr_2{\cdot}3H_2O$ (13.5 mM). In this experiment, the excited-state features and dynamics are remarkably similar to those observed when DABCO is the only quencher present (Figure 3E). While this result clearly demonstrates formation of Ir(II) **5** under the exact reaction conditions employed in our protocol, the absence of measurable reactivity toward the remaining reaction components suggests that either (i) Ir(II) **5** is not relevant to the catalytic activity or (ii) its role in initiation is necessary yet occurs with low quantum efficiency.

Role of Ir(II) in C−N Bond Formation. In considering the role that Ir(II) intermediate **5** might play in the dual-catalytic C−N coupling, we recognized that reduction of the Ni(II) precatalyst ($NiBr_2{\cdot}3H_2O$) to a low-valent form would be critical in facilitating the oxidative addition step in this C−N cross-coupling process. More specifically, a low-valent Ni(I) species would be competent to undergo oxidative addition with aryl bromide **2**, whereas its Ni(II) congener would be unable to undergo the prohibitively slow Ni(II)/Ni(IV) oxidative addition.[32] Within this mechanism, we reasoned that a plausible role for the identified Ir(II) intermediate would be in reducing the Ni(II) precatalyst to an active, low-valent Ni(I) form. To probe this hypothesis and interrogate the relevance of Ir(II) complex **5** to the overall dual-catalytic amination reaction, an array of Ir(III) photocatalysts (**1** and **6**−**12**) with systematically varied reduction potentials (ranging from $E_{1/2}^{red}[Ir^{III}/Ir^{II}] = -0.77$ V to −1.41 V) was employed in the reaction and the rate of product formation measured (Figure 4). In this SAR series, only highly reducing Ir(II)

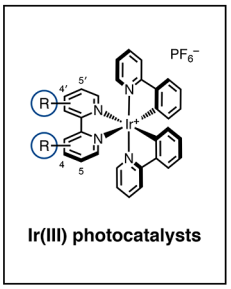

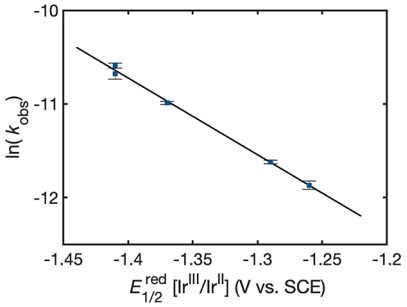

entry	photocatalyst	$E_{1/2}^{red}$ (V vs. SCE)	k_{obs} ($\mu M s^{-1}$)
1	$[Ir(ppy)_2(5,5'\text{-}Me_2bpy)]PF_6$ (**1**)	− 1.41	25.2(0.6)
2	$[Ir(ppy)_2(4,4'\text{-}(OMe)_2bpy)]PF_6$ (**6**)	− 1.41	23(1)
3	$[Ir(ppy)_2(4,4'\text{-}Me_2bpy)]PF_6$ (**7**)	− 1.37	16.9(0.2)
4	$[Ir(ppy)_2(bpy)]PF_6$ (**8**)	− 1.29	9.0(0.1)
5	$[Ir(ppy)_2(5,5'\text{-}F_2bpy)]PF_6$ (**9**)	− 1.26	7.0(0.3)
6	$[Ir(ppy)_2(4,4'\text{-}(CO_2Me)_2bpy)]PF_6$ (**10**)	− 0.90	NR
7	$[Ir(ppy)_2(4,4'\text{-}(CF_3)_2bpy)]PF_6$ (**11**)	− 0.88	NR
8	$[Ir(ppy)_2(5,5'\text{-}(CF_3)_2bpy)]PF_6$ (**12**)	− 0.77	NR

Figure 4. Structures and reduction potentials for a panel of Ir(III) photocatalysts and initial rate measurements for the photocatalytic C−N coupling between hexylamine and ArBr **2**. Error bars represent standard error of the mean (n = 2).

photocatalysts ($E_{1/2}^{red}[Ir^{III}/Ir^{II}] \leq -1.26$ V) gave rise to detectable levels of product formation (Figure 4), providing evidence that only sufficiently reducing Ir(II) species are able to effect the challenging precatalyst reduction step ($E_i[Ni^{II}/Ni^{I}] = -1.43$ V vs SCE, Figure S67, see page S31 for further discussion). Furthermore, the reducing power of the Ir(II) species was found to correlate significantly with reaction rate, wherein a plot of $\ln(k_{obs})$ vs $E_{1/2}^{red}[Ir^{III}/Ir^{II}]$ exhibits a linear relationship over a small driving force range of 150 meV (Figure 4). A plot of k_{obs} vs [Ni] (Figure S8) shows a strong rate dependence on the nickel concentration, a finding which is consistent with the Ir(II) intermediate directly reducing the Ni(II) precatalyst, given that the rate of single electron transfer between Ir(II) and Ni(II) should depend not only on the reducing power of Ir(II) but also on the concentration of Ni(II). Taking this latter result together with the strong dependence of the reaction rate on the Ir(II) reducing power

https://dx.doi.org/10.1021/jacs.0c05901
J. Am. Chem. Soc. 2020, 142, 15830−15841

(Figure 4) it appears evident that the Ir(II) intermediate is relevant to the overall photoredox C−N coupling and that the reduction of the Ni(II) precatalyst is likely involved in determining the overall rate of product formation.

In order to investigate the impact of the low-efficiency Ni reduction process on the resting states of the iridium and nickel catalysts, steady-state absorption measurements of the dual-catalytic amination were carried out. The absorption spectrum for the C−N coupling under the standard reaction conditions (following irradiation at 450 nm) bears remarkable similarity to the absorption spectrum reported for an analogous Ni(II) amine complex by Miyake and co-workers.[28] This led to a tentative assignment of the Ni(II) catalyst in this system as octahedral tetrakis(hexylamino)nickel(II) dibromide (**13**, Figure 5, orange trace). Moreover, the absorption spectrum

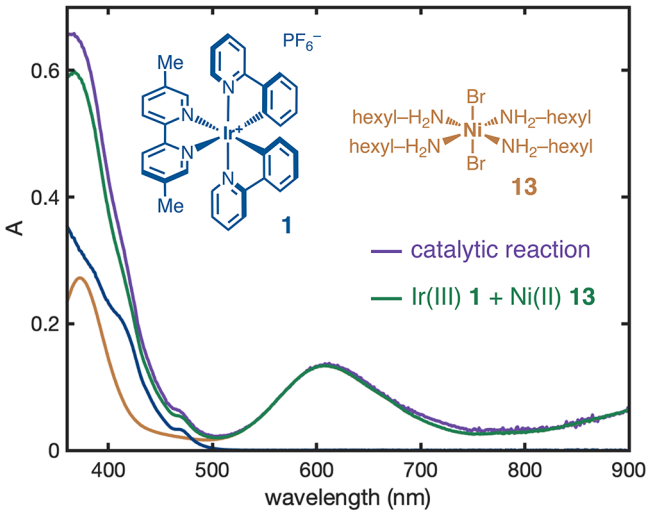

Figure 5. Steady-state UV−vis spectra of Ni(II) catalyst **13** (orange), Ir(III) photocatalyst **1** (blue), their linear combination (green), and full reaction mixture (purple) following 450 nm irradiation for 5 min.

for the complete C−N coupling protocol (containing all of the reaction components) can be reconstructed from a simple sum of independently measured Ni(II) and Ir(III) spectra (Figure 5, green and purple traces, respectively), confirming the resting states of the two metal catalysts as photocatalyst **1** and Ni(II) complex **13** (Figure 5). This finding, that the nickel catalyst exists predominantly in its Ni(II) oxidation state, is consistent with the spectroscopic observation that Ir(II) formation is efficient but that the subsequent Ni(II) reduction step is extremely inefficient. Furthermore, the spectroscopic evidence that photocatalyst **1** is predominantly in its ground-state Ir(III) form demonstrates that back electron transfer from Ir(II) to the DABCO radical cation is likely rapid, thereby preventing any buildup in concentration of the reduced Ir(II) species.

Mechanism of C−N Reductive Elimination. After studying the primary photochemical decay pathway of the excited-state iridium catalyst and its subsequent role in reductively initiating Ni catalysis, we turned our attention to understanding the precise nature of the Ni-catalyzed C−N bond-forming step. In particular, three general mechanisms are often invoked in Ni-catalyzed N- and O-arylation reactions: (A) a Ni(I)/Ni(III) cycle, which proceeds through Ni(I)/Ni(III) oxidative addition with the aryl halide partner and a subsequent Ni(III)/Ni(I) C−X (X = N, O) bond-forming reductive elimination (Figure 6A), (B) a Ni(0)/Ni(II) cycle, wherein the analogous Ni(0)/Ni(II) oxidative addition and Ni(II)/Ni(0) reductive eliminations take place (Figure 6B), or (C) a Ni(0)/Ni(II)/Ni(III)/Ni(I)/Ni(0) process, wherein Ni(0)/Ni(II) oxidative addition precedes a photocatalytic oxidatively induced reductive elimination and Ni(I)/Ni(0) reduction (Figure 6C).[23] Given the high efficiency of quenching Ir(III)* **4** by DABCO (Φ_q > 0.99), the photo-induced reductive elimination step implicated in mechanism C would likely proceed through electron relay, wherein $DABCO^{\bullet+}$ rather than Ir(III)* serves to oxidize the Ni(II) center. Precise mechanistic details on the Ni oxidation states implicated in these various potential pathways are often challenging to obtain, but pioneering stoichiometric work by Hillhouse[33] and more recent studies by Zargarian[34] have demonstrated that while Ni(II)/Ni(0) reductive elimination from Ni(II) amido complexes is slow at room temperature, their Ni(III) oxidation state congeners undergo rapid C−N bond formation with the same thermal exposure. This stark contrast in bond-formation rates suggests the Ni(III) oxidation state may be responsible for promoting the otherwise challenging C−N bond-formation step in the presently studied amination reaction, especially considering the absence of a ligand designed for facilitating C−N reductive elimination.[35] In order to probe the role of the Ni(II) or Ni(III) oxidation state in promoting C−N reductive elimination, stoichiometric organometallic studies with Ni complexes bearing catalytically relevant ligand spheres were undertaken. To this end, Ni(II) amine complexes **14** and **15** with two different amine coupling partners were prepared. These Ni(II) complexes can be prepared in 3 steps or fewer (Scheme S2) and are indefinitely stable in the solid form.

Moreover, they are stable toward C−N reductive elimination in DMF solution both in the dark and under 450 nm irradiation (Tables S7 and S8). Cyclic voltammetry was then employed to examine the oxidative stabilities of Ni(II) complexes **14** and **15**: both complexes display irreversible oxidation waves (E_i = +0.70 and +0.69 V vs SCE for **14** and **15**, respectively). This electrochemical behavior begged the question of whether a rapid intramolecular reductive elimination process after oxidation at the electrode serves as the chemical basis for the irreversible nature of the two oxidation events (Figure 6D). To test this hypothesis, Ni(II) complexes **14** and **15** were treated with a mild single-electron oxidant ($FcBF_4$, ferrocenium tetrafluoroborate, $E_{1/2}^{red}[Fe^{III}/Fe^{II}]$ = +0.49 V vs SCE). Under these conditions, both **14** and **15** undergo efficient reductive elimination to give the expected C−N coupled products (**16** and **17**) within minutes (68% yield of **16** from **14** and 70% yield of **17** from **15**, Figure 6E). These results underscore the rapid nature with which C−N bond formation can take place under the appropriate conditions and the importance of accessing the Ni(III) oxidation state in promoting this elementary organometallic step. In the context of mechanisms A−C, a key feature distinguishing mechanisms A and C from mechanism B lies in the details of the reductive elimination process. Mechanism B relies on a Ni(II)/Ni(0) reductive elimination to forge the C−N coupled product, which is apparently a low-efficiency step under these conditions. In contrast, both mechanisms A and C remain as plausible pathways given the high efficiency of reductive elimination from Ni(III).

In considering the two mechanisms involving C−N reductive elimination from Ni(III) (mechanisms A and C), we first evaluated mechanism C in a stoichiometric setting. In

https://dx.doi.org/10.1021/jacs.0c05901
J. Am. Chem. Soc. 2020, 142, 15830−15841

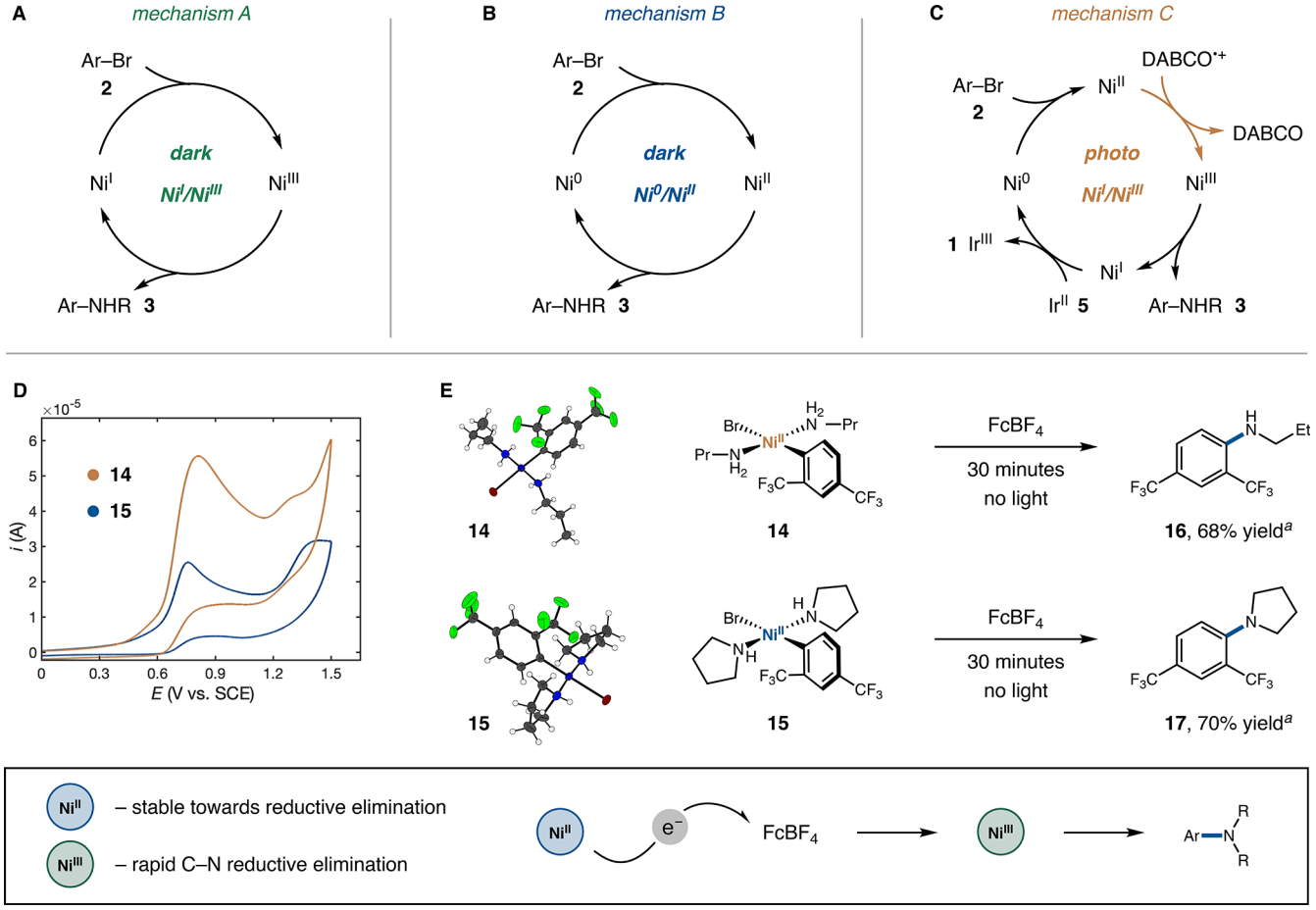

Figure 6. (A) General Ni(I)/Ni(III) cross-coupling mechanism showing elementary steps involved in oxidation state changes. (B) General Ni(0)/Ni(II) cross-coupling mechanism. (C) General Ni(0)/Ni(II)/Ni(III)/Ni(I) mechanism involving photoinduced reductive elimination. (D) Cyclic voltammetry data for Ni(II) aryl amine complexes **14** and **15** in DMF (0.1 M NBu_4PF_6). (E) Solid state structures and oxidatively induced reductive elimination reactions with independently synthesized Ni(II) aryl amine complexes **14** and **15**. ORTEP structures with 70% probability ellipsoids (*para*-CF_3 groups disorder omitted for clarity). [a]Yields determined by ^{19}F NMR.

order to access the Ni(III) oxidation state, mechanism C invokes a photoinduced oxidation process from an intermediate Ni(II) complex (Figure 6C). To assess the viability of this photoinduced reductive elimination step, Ni(II) complex **14** was exposed to photocatalyst **1**, 450 nm irradiation, and catalytically relevant concentrations of amine and DABCO. At the high amine concentration relevant to the catalytic conditions (405 mM), nickel complex **14** is present predominantly in its cationic tris(amino) aryl bromide form, **18** (Figure S42). Under these conditions, Ni(II) complex **18** undergoes efficient C–N coupling to give aniline **16** (Figure 7, 69% yield), and control experiments reveal that amine association does not dramatically affect this reductive elimination efficiency (Tables S7 and S10). In total, this result clearly demonstrates that photocatalyst **1** is capable of inducing C–N bond formation from an otherwise stable Ni(II) aryl

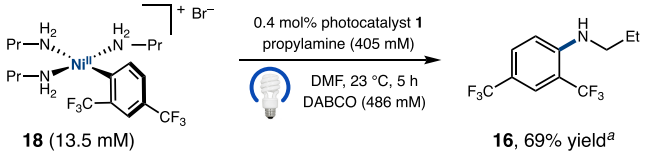

Figure 7. Stoichiometric photoinduced reductive elimination with Ni(II) complex **18**. [a]Yield determined by ^{19}F NMR.

amine complex, a step which is crucial to the viability of mechanism C (Figure 6C).

Unfortunately, based on stoichiometric reductive elimination experiments alone, mechanisms A and C still cannot be distinguished. Instead, closer examination of the quantum efficiencies of C–N cross-coupling and those of the component mechanistic steps leading to the final product enables discrimination between the two competing mechanisms. In more detail, a relationship can be constructed between the quantum yields of overall product formation (Φ_{tot}), Ir(III)* quenching to form Ir(II) (Φ_q), Ni catalyst initiation by Ir(II) (Φ_{Ir}), and that of the product-forming nickel-catalyzed process (Φ_{Ni}). In this relationship, the total quantum yield of product formation (Φ_{tot}) should be equivalent to the product of quantum yields for the individual components of the catalytic mechanism (Φ_q, Φ_{Ir}, and Φ_{Ni}, Figure 8). A key feature distinguishing mechanisms A and C lies in the necessity for light input in mechanism C to achieve catalyst turnover, whereas mechanism A requires no photonic input beyond the initiation step. In terms of theoretical maxima for quantum efficiencies of these processes (Φ_{Ni}), mechanism C requires one photon per turnover, limiting its maximum quantum yield to 1 ($\Phi_{Ni} \leq 1$), whereas mechanism A has no theoretical limit in this regard. On the basis of this analysis, obtaining the quantum yield of the Ni-catalyzed

https://dx.doi.org/10.1021/jacs.0c05901
J. Am. Chem. Soc. 2020, 142, 15830–15841

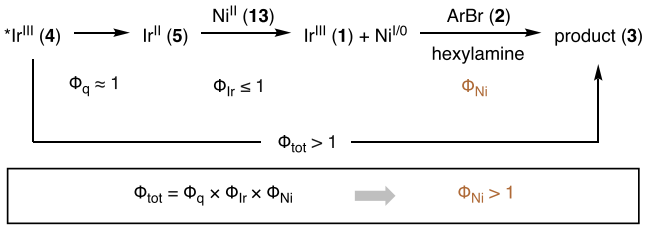

Figure 8. Schematic representation of mechanistic components of photoredox C−N coupling and associated quantum yields.

product-forming cycle within the photoredox C−N coupling (Φ_{Ni}) could provide a straightforward means for differentiating between the two general mechanisms. In particular, a quantum yield for the nickel cycle above 1 ($\Phi_{Ni} > 1$) would indicate that mechanism C is not the only operative mechanism, and a quantum yield significantly surpassing unity would indicate that C can only be minimally operative.

In order to make an assessment of Φ_{Ni} based on the aforementioned analysis, measurements and estimates for all quantum yield values aside from Φ_{Ni} were carried out. We first recognized that the Ir(III)* quenching efficiency by DABCO is sufficiently high to be disregarded in the calculation (Φ_q > 0.99, Figure 2A). While a quantitative evaluation of Φ_{Ir} cannot be made based on the lack of observable Ni(II) reduction by pump−probe measurements (Figure 3E, Figure S46B), this value necessarily has an upper bound of 1 and is likely considerably lower based on the absence of quenching in comparing the transient absorption decay kinetics of Ir(II) **5** with and without Ni(II) (Figure S46B). While in the case of mechanism A single electron transfer between Ir(II) and Ni(II) would directly produce Ni(I), subsequent disproportionation[36] or further reduction would be required to access Ni(0) in mechanism C. This added mechanistic complexity makes the upper bound for Φ_{Ir} in mechanism C lower than the corresponding value for mechanism A but does not affect the final analysis. Finally, Φ_{tot} can be measured through standard reaction kinetics measurements and chemical actinometry (Φ_{tot} up to 1.1 for hexylamine coupling, Tables S3 and S4, and 5.4 for pyrrolidine coupling, Table S4). Taking these values together reveals that Φ_{Ni} is greater than unity ($\Phi_{Ni} \geq 1.1$ for hexylamine and $\Phi_{Ni} \geq 5.4$ for pyrrolidine). Moreover, the vanishingly low value for Φ_{Ir} indicated by the Ni(II)-quenched transient absorption spectroscopy measurements suggests that Φ_{Ni} significantly passes the theoretical limit for a one-photon-per-turnover mechanism. This result not only rules out mechanism C as the only mechanism but also makes clear that this mechanism can only be minimally responsible for product formation. Moreover, this highly efficient nickel-catalyzed product formation pathway is consistent with mechanism A, which requires no photonic input for turnover. More specifically, this finding indicates that while inefficient Ni(II) reduction by Ir(II) hampers formation of high concentrations of active Ni(I), the activated nickel catalyst is able to undergo multiple turnovers to arrive at high overall total quantum efficiencies ($\Phi_{tot} > 1$).

Role of C−Br Oxidative Addition. While the aforementioned spectroscopic and kinetic evidence demonstrates the importance of Ni(II) reduction by Ir(II) intermediate **5** in promoting the C−N cross-coupling and stoichiometric reductive elimination experiments suggest the C−N bond-forming step is efficient and rapid, it is unclear from these studies what role the oxidative addition step plays in determining the reaction efficiency. To better understand the impact of this elementary organometallic step on the efficiency of C−N coupling, we examined the influence of aryl halide electronics on the reaction rate. Initial rates of product formation were measured for a variety of electronically diverse 4-substituted aryl bromides. A Hammett correlation could be constructed from these measurements, giving a strong positive correlation (ρ = +4.5), indicating that during the Ni(I)/Ni(III) oxidative addition transition state there is significant negative charge buildup on the electrophilic aryl bromide and that this oxidative addition step plays a significant role in determining the overall rate of C−N coupling (Figure 9).[37]

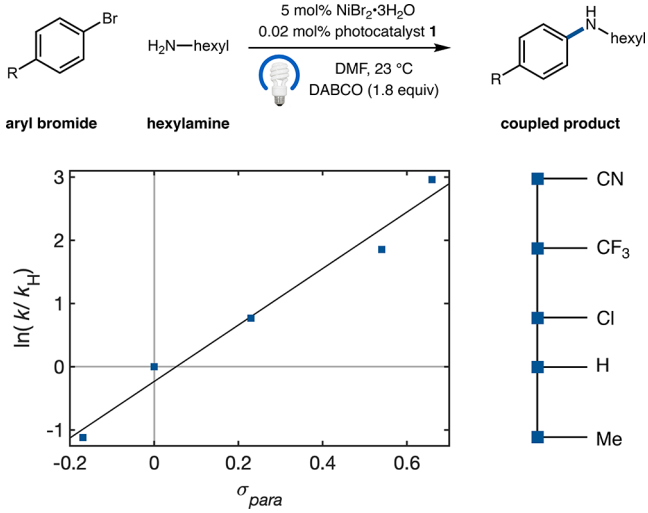

Figure 9. Dependence of the rate of C−N coupling on the aryl bromide para-substituent Hammett electronic parameter.

This finding is consistent with a mechanistic scenario in which the active Ni(I) species can either undergo oxidative addition, or a competitive oxidative deactivation process, such as oxidation by DABCO$^{\bullet+}$, or comproportionation with Ni(III), either of which would convert this Ni(I) species back into the observed Ni(II) resting state, **13**. Within this competition, increasing σ_p values for the aryl bromide partner would favor the desired oxidative addition pathway, thus resulting in higher quantum yields of product formation (Table S4).

Catalyst Development Studies. Taken together, these spectroscopic investigations, stoichiometric experiments, and kinetic studies demonstrate the photochemical mechanism for Ni cocatalyst activation by Ir(III) photocatalyst **1** and further support a Ni(I)/Ni(III) cycle as being responsible for the ensuing C−N bond-formation step (Figure 10A). In more detail, photocatalyst **1** accesses an oxidizing excited state under 450 nm irradiation ($E_{1/2}^{red}[Ir^{III}*/Ir^{II}]$ = +1.08 V vs SCE), which subsequently undergoes rapid exergonic electron transfer quenching with DABCO ($k_{ET} = 1.34 \times 10^9$ s^{-1}, ΔG = −0.37 eV), giving rise to long-lived (>100 μs) Ir(II) state **5** and DABCO$^{\bullet+}$ (Figure 10A). While this Ir(II) intermediate predominantly undergoes a highly exergonic charge recombination with DABCO$^{\bullet+}$ (ΔG = −2.12 eV), its reduction of Ni(II) catalyst **13** ($\Delta G \approx 0$ eV), albeit with low efficiency, initiates a Ni(I)/Ni(III) cycle responsible for C−N bond formation between the amine and the aryl halide coupling partners. In particular, Ni(I) species **19** (produced through reduction by Ir(II)) can undergo C−Br oxidative addition with aryl bromide **2** and C−N bond-forming reductive elimination

https://dx.doi.org/10.1021/jacs.0c05901
J. Am. Chem. Soc. 2020, 142, 15830−15841

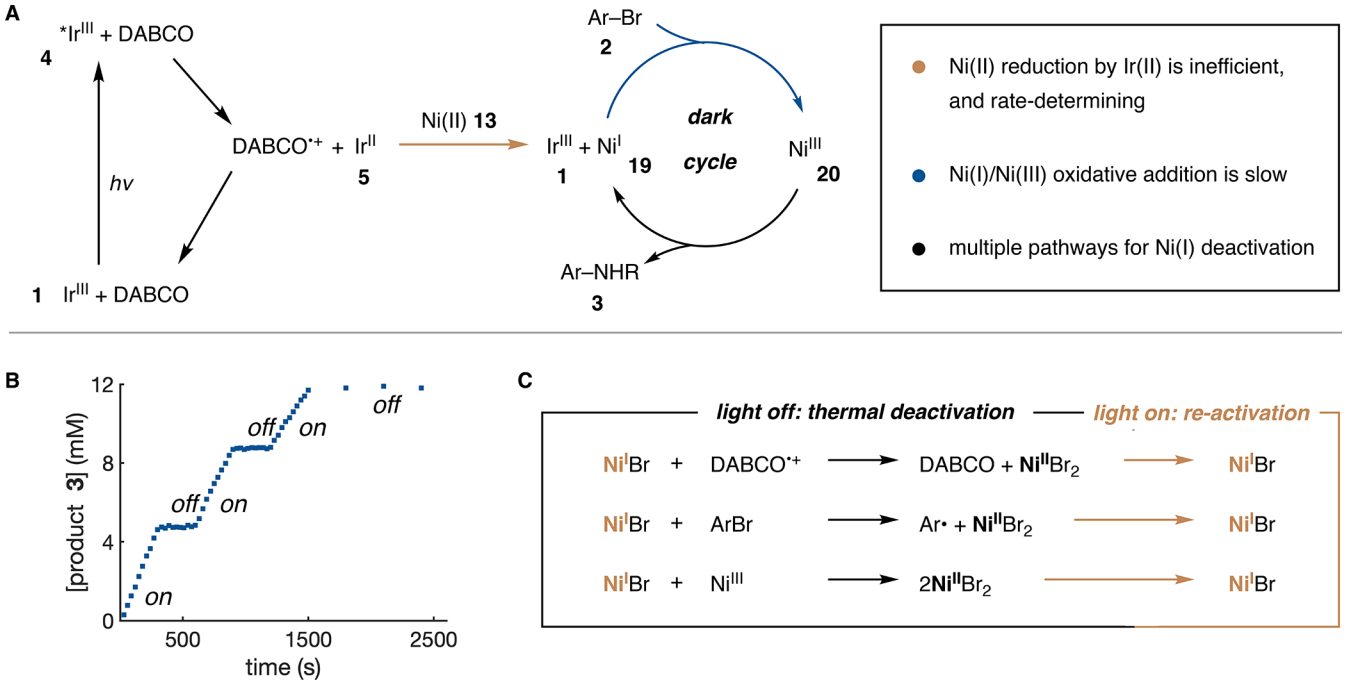

Figure 10. (A) Overview of photochemical and organometallic mechanisms underlying photoredox C–N coupling with rate-determining steps highlighted (orange and blue). (B) Plot of product concentration vs time with and without irradiation where indicated (440 nm, photoNMR). (C) Proposed mechanisms for oxidative deactivation of active Ni(I) catalyst. See Figure S48 for further details.

with bound hexylamine to furnish the coupled product **3**. In this process, the reductive elimination step is rapid, whereas oxidative addition is slow and impacts the overall rate of coupling.

Having determined the role of the photocatalyst in initiating the nickel-catalyzed cross-coupling process, we questioned whether the resulting Ni(I)/Ni(III) cycle could perpetuate continuously without further irradiation given that no photonic input is required for Ni catalyst turnover (Figure 10A). To probe this hypothesis, the light dependence of the reaction was examined. Product formation rapidly ceases in the absence of light, indicating that the Ni(I)/Ni(III) cycle does not continuously perpetuate under these conditions and instead deactivates rapidly (<30 s) (Figure 10B). This finding is consistent with the vanishingly low level of Ni(I) buildup (below the detection limit) observed by steady-state UV–vis spectroscopy during the course of the reaction (Figure 5). While the deactivation mechanisms at play in the Ni(I)/Ni(III) cycle are not entirely clear, electron recombination between the Ni(I) catalyst and DABCO$^{\bullet+}$, halogen-atom abstraction from aryl halide **2** by Ni(I) **19**,[38] and Ni(I)/Ni(III) comproportionation would all return the Ni(II)Br_2 resting state **13** observed spectroscopically (Figure 10C).

Recognizing that reduction of Ni(II) complex **13** is crucial not only to initiate the nickel-catalyzed cross-coupling mechanism but also in perpetuating this process, we endeavored to increase the efficiency of Ni(II) reduction through photocatalyst design (Figure 11). More specifically, Ir(III) photocatalysts of increasing electron density on the π^*-localized bipyridine ligand were prepared, and their photophysical and electrochemical properties were characterized. These new photocatalysts exhibit the expected increase in reducing power ($E_{1/2}^{red}[Ir^{III}/Ir^{II}]$ = −1.52 to −1.91 V vs SCE, Table S2) while still maintaining sufficient oxidizing powers to render quenching by DABCO exergonic ($E_{1/2}^{red}[Ir^{III*}/Ir^{II}]$ =

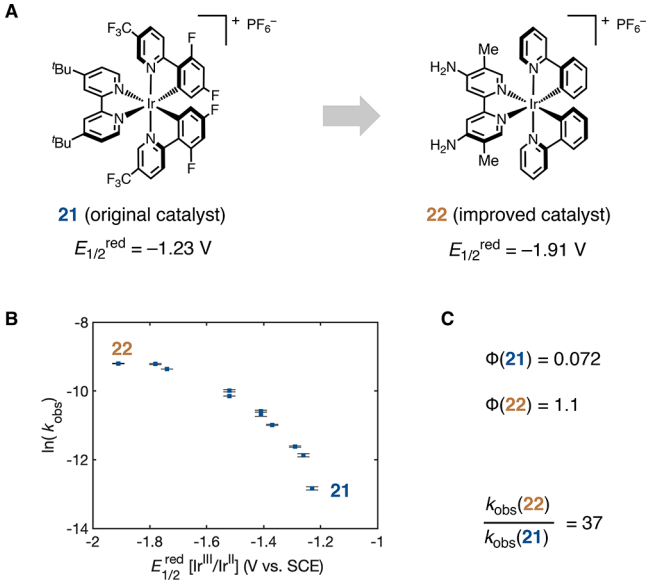

Figure 11. (A) Structures and reduction potentials for originally reported catalyst **21** and improved catalyst **22**. (B) Plot of ln(k_{obs}) vs Ir(III)/Ir(II) reduction potential over a large driving force range (680 meV) including new photocatalysts. (C) Comparison of the C–N coupling performance of catalysts **21** and **22** with 4-bromobenzotrifluoride and hexylamine coupling partners. Error bars represent standard error of the mean (n = 2).

+1.05 to +0.73 V vs SCE, Table S2). In accordance with the overall mechanistic hypothesis, iridium photocatalysts with lower reduction potentials and hence higher driving forces for Ni(II) reduction should give rise to higher rates of product formation provided that these catalysts are simultaneously sufficiently oxidizing to access their Ir(II) forms through DABCO oxidation. In such a rate–driving force relationship,

https://dx.doi.org/10.1021/jacs.0c05901
J. Am. Chem. Soc. 2020, 142, 15830–15841

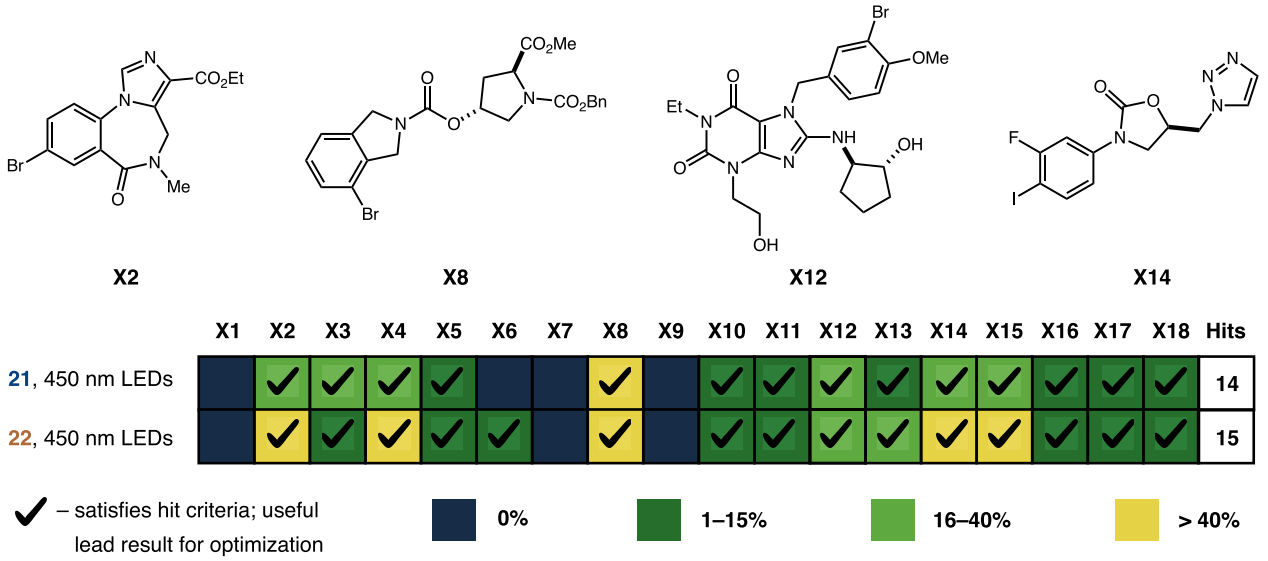

Figure 12. Product formation levels for the cross-coupling reaction of piperidine with the 18 aryl halide informer library members under light-mediated photoredox conditions with photocatalysts **21** and **22**, and structures of selected library members shown above.

increased reaction rate would be expected to accompany reducing power increases until a curve flattening as the diffusion limit for electron transfer is reached. Indeed, these new catalysts gave rise to higher levels of reaction efficiency, culminating in a 37-fold increase in the initial rate and >10-fold increase in the quantum yield of product formation with catalyst **22** when compared to photocatalyst **21**, originally reported for the photoredox C–N coupling (Figure 11A–C). Moreover, photocatalyst **22** provides a significantly improved full reaction course profile (Figure S18). These studies provide guiding principles for photocatalyst design directed toward both initiating and perpetuating Ni(I)/Ni(III) cross-coupling activity.

Having explored the mechanistic underpinnings of the photoredox aryl amination and developed a higher efficiency photocatalyst for this cross-coupling reaction, we next turned our attention to examining the relevance of these mechanistic insights to end-user medicinal chemistry applications of C–N cross-coupling. The importance of C–N cross-coupling to medicinal chemistry applications in particular has motivated mechanistic studies on this class of reactions historically with Pd-catalyzed methods[39] and more recently in the context of nickel catalysis.[40,41] On the basis of this, it became clear that for the mechanistic insights gained from this study to have the most relevance, their applicability in complex, drug-like settings would need to be demonstrated. More specifically, the presence of numerous heteroatoms, sensitive functional groups, and other metal-coordinating sites in pharmaceutical compounds and their synthetic precursors requires that a robust cross-coupling method carry out the desired bond-forming process without interference from a diverse set of competing functionalities. Taking this consideration together with our catalyst optimization studies makes it clear that while photocatalyst **22** operates with a higher rate and quantum efficiency than its predecessor with a set of model substrates (Figure 11), its generality would be of crucial importance in determining its superiority as a photocatalyst for C–N cross-coupling.

Over the past 5 years, a set of 18 particularly challenging aryl halide cross-coupling partners constructed by Dreher and co-workers (referred to as an informer library) has emerged as a standardized means for benchmarking the generality of new metal-catalyzed cross-coupling protocols.[42] This set of aryl halide substrates was specifically constructed based on the molecular complexities of the cross-coupling partners, including many potential metal coordination sites and reactive functionalities (Figure S43). This effort resulted in a set of aryl halides with molecular complexity mirroring that of drug substances and intermediates, making this evaluation technique particularly relevant to medicinal chemistry applications. Given these properties, we recognized that this benchmarking technique would be an apt method for evaluating the generality of photocatalyst **22**. To this end, C–N coupling reactions with each member of the aryl halide informer library were carried out with photocatalyst **22**. Gratifyingly, the desired C–N-coupled products are obtained with the vast majority of aryl halide library members under these photocatalytic conditions (15 of 18 aryl halides). While a number of these aryl halides give rise to only low levels of product formation (1–15% yield, Figure S43) under the action of photocatalyst **22**, these results serve as promising leads for further optimization given that medicinal chemistry campaigns often originate from low but nonzero levels of product formation. In comparing the performance of catalyst **22** to that of the originally reported catalyst **21**, the redesigned photocatalyst **22** gives broadly similar levels of reactivity across the informer library but with modestly expanded generality (**X6** can be coupled with catalyst **22** but not **21**, Figure 12). In total, improved photocatalyst **22** exhibits a dramatically improved reaction rate and quantum efficiency without sacrificing the generality of the originally reported photoredox C–N coupling protocol. Within the context of larger scale applications of C–N coupling, a recent report by Corcoran et al. on the kilogram-scale application of this photoredox amination in flow further highlights the importance of minimizing residence time and energy input by maximizing reaction rate and quantum yield, respectively.[24]

While the precise mechanistic details underlying the high generality of the photoredox C–N cross-coupling are not entirely clear at present, light-mediated formation of the active Ni(I) catalyst rather than stoichiometric reduction to low-

https://dx.doi.org/10.1021/jacs.0c05901
J. Am. Chem. Soc. 2020, 142, 15830–15841

valent nickel appears to enable high C−N cross-coupling activity across a diverse set of aryl halide partners. Mechanistically, the use of an appropriate photocatalyst and visible light irradiation may provide a route for continual generation of a highly active Ni(I) catalyst capable of carrying out challenging oxidative addition steps, even if this catalyst often returns to its Ni(II) resting state **13** through the aforementioned deactivation mechanisms (Figure 10C). More specifically, maintaining a low concentration of active Ni(I) may disfavor bimolecular dimerization and further aggregation to form nickel-black, a process which has recently been shown to detrimentally affect nickel-catalyzed C−N cross-coupling efficiency.[43] By avoiding the formation of unreactive nickel-black, this photocatalytic mode of catalyst activation generates a highly active low-valent nickel complex capable of performing challenging oxidative addition steps with relatively unreactive aryl halides and in the presence of multiple coordinating functional groups (Figure 12). Beyond these specific mechanistic features, the use of photocatalysis more broadly provides an opportunity to systematically tune the electrochemical and photophysical properties of the photocatalyst for a given C−N cross-coupling reaction as demonstrated in our photocatalyst SAR studies (Figure 11). This feature serves as a point of modularity, akin to the use of ligand modulation which has rendered Pd-catalyzed C−N coupling so robust in medicinally relevant contexts.

CONCLUSION

The use of steady-state and time-resolved spectroscopic techniques has long provided a powerful approach to elucidating photophysical and photochemical reaction mechanisms. At the same time, traditional kinetic and stoichiometric experiments are often employed to gain important mechanistic insight into synthetically important transition-metal-catalyzed cross-coupling reactions. In this study, their combined use has proven particularly advantageous, wherein this multifaceted approach has helped uncover the photochemical and organometallic mechanisms underlying the nickel/photoredox dual-catalytic amination of aryl bromides. Of particular relevance to the practicing organic chemist, these studies have demonstrated the role of photocatalysis in this C−N cross-coupling reaction: not only does the photocatalyst initiate the reaction through Ni(II) reduction but also its presence ensures that reactivity perpetuates through continually reducing the resting-state Ni(II) catalyst to its active, low-valent form. Moreover, analysis of the overall quantum yield of product formation and low quantum yield of initiation reveals that the active Ni catalyst in this system operates at high efficiency. These studies have further pinpointed the inefficient catalytic steps present in this C−N cross-coupling reaction, knowledge which proved indispensable in designing new photocatalysts capable of superior performance in a synthetically meaningful context. Overall, this study may provide a roadmap to mechanistic analysis and catalyst improvement in the context of dual-catalytic photoredox cross-coupling reactions.

ASSOCIATED CONTENT

Supporting Information

The Supporting Information is available free of charge at https://pubs.acs.org/doi/10.1021/jacs.0c05901.

Experimental procedures, characterization data, and spectroscopic data (PDF)

Crystallographic data for **15** (CIF)

Crystallographic data for **18** (CIF)

Crystallographic data for **14** (CIF)

AUTHOR INFORMATION

Corresponding Author

David W. C. MacMillan − *Merck Center for Catalysis at Princeton University, Princeton, New Jersey 08544, United States;* orcid.org/0000-0001-6447-0587; Email: dmacmill@princeton.edu

Authors

Nicholas A. Till − *Merck Center for Catalysis at Princeton University, Princeton, New Jersey 08544, United States;* orcid.org/0000-0003-2421-7186

Lei Tian − *Department of Chemistry, Princeton University, Princeton, New Jersey 08544, United States*

Zhe Dong − *Merck Center for Catalysis at Princeton University, Princeton, New Jersey 08544, United States*

Gregory D. Scholes − *Department of Chemistry, Princeton University, Princeton, New Jersey 08544, United States;* orcid.org/0000-0003-3336-7960

Complete contact information is available at: https://pubs.acs.org/10.1021/jacs.0c05901

Notes

The authors declare no competing financial interest.

ACKNOWLEDGMENTS

This work was supported as part of BioLEC, an Energy Frontier Research Center funded by the U.S. Department of Energy, Office of Science under Award # DE-SC0019370 and kind gifts from Merck, BMS, Pfizer, Janssen, Genentech, and Eli Lilly. We acknowledge the Princeton Catalysis Initiative for supporting this work. N.A.T. and L.T. acknowledge Princeton University, E. Taylor, and the Taylor family for an Edward C. Taylor Fellowship. We thank Phil Jeffrey of Princeton University for X-ray crystallographic structure determination. We thank Megan H. Shaw and Emily B. Corcoran for their help in carrying out initial studies.

REFERENCES

(1) Miyaura, N.; Suzuki, A. Palladium-Catalyzed Cross-Coupling Reactions of Organoboron Compounds. *Chem. Rev.* **1995**, *95* (7), 2457−2483.

(2) Johansson Seechurn, C. C. C.; Kitching, M. O.; Colacot, T. J.; Snieckus, V. Palladium-Catalyzed Cross-Coupling: A Historical Contextual Perspective to the 2010 Nobel Prize. *Angew. Chem., Int. Ed.* **2012**, *51* (21), 5062−5085.

(3) Torborg, C.; Beller, M. Recent Applications of Palladium-Catalyzed Coupling Reactions in the Pharmaceutical, Agrochemical, and Fine Chemical Industries. *Adv. Synth. Catal.* **2009**, *351* (18), 3027−3043.

(4) Miura, M. Rational Ligand Design in Constructing Efficient Catalyst Systems for Suzuki−Miyaura Coupling. *Angew. Chem., Int. Ed.* **2004**, *43* (17), 2201−2203.

(5) Lundgren, R. J.; Stradiotto, M. Addressing Challenges in Palladium-Catalyzed Cross-Coupling Reactions Through Ligand Design. *Chem. - Eur. J.* **2012**, *18* (32), 9758−9769.

(6) Bruno, N. C.; Tudge, M. T.; Buchwald, S. L. Design and Preparation of New Palladium Precatalysts for C−C and C−N Cross-Coupling Reactions. *Chem. Sci.* **2013**, *4* (3), 916−920.

(7) Joost, M.; Zeineddine, A.; Estévez, L.; Mallet-Ladeira, S.; Miqueu, K.; Amgoune, A.; Bourissou, D. Facile Oxidative Addition of

Aryl Iodides to Gold(I) by Ligand Design: Bending Turns on Reactivity. *J. Am. Chem. Soc.* **2014**, *136* (42), 14654−14657.
(8) Clarke, M. L.; Frew, J. J. R. Ligand Electronic Effects in Homogeneous Catalysis Using Transition Metal Complexes of Phosphine Ligands. *Organometallic Chemistry* **2009**, *35*, 19−46.
(9) Nielsen, M. C.; Bonney, K. J.; Schoenebeck, F. Computational Ligand Design for the Reductive Elimination of ArCF3 from a Small Bite Angle PdII Complex: Remarkable Effect of a Perfluoroalkyl Phosphine. *Angew. Chem., Int. Ed.* **2014**, *53* (23), 5903−5906.
(10) Ruiz-Castillo, P.; Blackmond, D. G.; Buchwald, S. L. Rational Ligand Design for the Arylation of Hindered Primary Amines Guided by Reaction Progress Kinetic Analysis. *J. Am. Chem. Soc.* **2015**, *137* (8), 3085−3092.
(11) Hartwig, J. F. Palladium-Catalyzed Amination of Aryl Halides: Mechanism and Rational Catalyst Design. *Synlett* **1997**, *1997* (4), 329−340.
(12) Olsen, E. P. K.; Arrechea, P. L.; Buchwald, S. L. Mechanistic Insight Leads to a Ligand Which Facilitates the Palladium-Catalyzed Formation of 2-(Hetero)Arylaminooxazoles and 4-(Hetero)-Arylaminothiazoles. *Angew. Chem., Int. Ed.* **2017**, *56* (35), 10569−10572.
(13) Klinkenberg, J. L.; Hartwig, J. F. Slow Reductive Elimination from Arylpalladium Parent Amido Complexes. *J. Am. Chem. Soc.* **2010**, *132* (34), 11830−11833.
(14) Dennis, J. M.; White, N. A.; Liu, R. Y.; Buchwald, S. L. Breaking the Base Barrier: An Electron-Deficient Palladium Catalyst Enables the Use of a Common Soluble Base in C−N Coupling. *J. Am. Chem. Soc.* **2018**, *140* (13), 4721−4725.
(15) Dennis, J. M.; White, N. A.; Liu, R. Y.; Buchwald, S. L. Pd-Catalyzed C−N Coupling Reactions Facilitated by Organic Bases: Mechanistic Investigation Leads to Enhanced Reactivity in the Arylation of Weakly Binding Amines. *ACS Catal.* **2019**, *9*, 3822−3830.
(16) Tellis, J. C.; Primer, D. N.; Molander, G. A. Single-Electron Transmetalation in Organoboron Cross-Coupling by Photoredox/Nickel Dual Catalysis. *Science* **2014**, *345* (6195), 433−436.
(17) Kainz, Q. M.; Matier, C. D.; Bartoszewicz, A.; Zultanski, S. L.; Peters, J. C.; Fu, G. C. Asymmetric Copper-Catalyzed C-N Cross-Couplings Induced by Visible Light. *Science* **2016**, *351* (6274), 681−684.
(18) Terrett, J. A.; Cuthbertson, J. D.; Shurtleff, V. W.; MacMillan, D. W. C. Switching on Elusive Organometallic Mechanisms with Photoredox Catalysis. *Nature* **2015**, *524* (7565), 330.
(19) Welin, E. R.; Le, C.; Arias-Rotondo, D. M.; McCusker, J. K.; MacMillan, D. W. C. Photosensitized, Energy Transfer-Mediated Organometallic Catalysis through Electronically Excited Nickel(II). *Science* **2017**, *355* (6323), 380−385.
(20) Liang, Y.; Zhang, X.; MacMillan, D. W. C. Decarboxylative Sp 3 C−N Coupling via Dual Copper and Photoredox Catalysis. *Nature* **2018**, *559* (7712), 83−88.
(21) Le, C.; Chen, T. Q.; Liang, T.; Zhang, P.; MacMillan, D. W. C. A Radical Approach to the Copper Oxidative Addition Problem: Trifluoromethylation of Bromoarenes. *Science* **2018**, *360* (6392), 1010−1014.
(22) Kim, S.; Toste, F. D. Mechanism of Photoredox-Initiated C−C and C−N Bond Formation by Arylation of IPrAu(I)−CF3 and IPrAu(I)−Succinimide. *J. Am. Chem. Soc.* **2019**, *141* (10), 4308−4315.
(23) Corcoran, E. B.; Pirnot, M. T.; Lin, S.; Dreher, S. D.; DiRocco, D. A.; Davies, I. W.; Buchwald, S. L.; MacMillan, D. W. C. Aryl Amination Using Ligand-Free Ni(II) Salts and Photoredox Catalysis. *Science* **2016**, *353* (6296), 279−283.
(24) Corcoran, E. B.; McMullen, J. P.; Lévesque, F.; Wismer, M. K.; Naber, J. R. Photon Equivalents as a Parameter for Scaling Photoredox Reactions in Flow: Translation of Photocatalytic C−N Cross-Coupling from Lab Scale to Multikilogram Scale. *Angew. Chem., Int. Ed.* **2020**, *59* (29), 11964−11968.
(25) Lowry, M. S.; Goldsmith, J. I.; Slinker, J. D.; Rohl, R.; Pascal, R. A.; Malliaras, G. G.; Bernhard, S. Single-Layer Electroluminescent Devices and Photoinduced Hydrogen Production from an Ionic Iridium(III) Complex. *Chem. Mater.* **2005**, *17* (23), 5712−5719.
(26) Arias-Rotondo, D. M.; McCusker, J. K. The Photophysics of Photoredox Catalysis: A Roadmap for Catalyst Design. *Chem. Soc. Rev.* **2016**, *45* (21), 5803−5820.
(27) Tian, L.; Till, N. A.; Kudisch, B.; MacMillan, D. W. C.; Scholes, G. D. Transient Absorption Spectroscopy Offers Mechanistic Insights for an Iridium/Nickel-Catalyzed C−O Coupling. *J. Am. Chem. Soc.* **2020**, *142* (10), 4555−4559.
(28) Kudisch, M.; Lim, C.-H.; Thordarson, P.; Miyake, G. M. Energy Transfer to Ni-Amine Complexes in Dual Catalytic, Light-Driven C−N Cross-Coupling Reactions. *J. Am. Chem. Soc.* **2019**, *141* (49), 19479−19486.
(29) Sun, R.; Qin, Y.; Ruccolo, S.; Schnedermann, C.; Costentin, C.; Nocera, D. G. Nocera. Elucidation of a Redox-Mediated Reaction Cycle for Nickel-Catalyzed Cross Coupling. *J. Am. Chem. Soc.* **2019**, *141* (1), 89−93.
(30) Shields, B. J.; Kudisch, B.; Scholes, G. D.; Doyle, A. G. Long-Lived Charge-Transfer States of Nickel(II) Aryl Halide Complexes Facilitate Bimolecular Photoinduced Electron Transfer. *J. Am. Chem. Soc.* **2018**, *140* (8), 3035−3039.
(31) Balakrishnan, G.; Keszthelyi, T.; Wilbrandt, R.; Zwier, J. M.; Brouwer, A. M.; Buma, W. J. The Radical Cation and Lowest Rydberg States of 1,4-Diaza[2.2.2]Bicyclooctane (DABCO). *J. Phys. Chem. A* **2000**, *104* (9), 1834−1841.
(32) Bour, J. R.; Camasso, N. M.; Sanford, M. S. Oxidation of Ni(II) to Ni(IV) with Aryl Electrophiles Enables Ni-Mediated Aryl−CF3 Coupling. *J. Am. Chem. Soc.* **2015**, *137* (25), 8034−8037.
(33) Koo, K.; Hillhouse, G. L. Carbon-Nitrogen Bond Formation by Reductive Elimination from Nickel(II) Amido Alkyl Complexes. *Organometallics* **1995**, *14* (9), 4421−4423.
(34) Cloutier, J.-P.; Zargarian, D. Functionalization of the Aryl Moiety in the Pincer Complex (NCN)NiIIIBr2: Insights on NiIII-Promoted Carbon−Heteroatom Coupling. *Organometallics* **2018**, *37* (9), 1446−1455.
(35) Lavoie, C. M.; Stradiotto, M. Bisphosphines: A Prominent Ancillary Ligand Class for Application in Nickel-Catalyzed C−N Cross-Coupling. *ACS Catal.* **2018**, *8* (8), 7228−7250.
(36) Beattie, D. D.; Lascoumettes, G.; Kennepohl, P.; Love, J. A.; Schafer, L. L. Disproportionation Reactions of an Organometallic Ni(I) Amidate Complex: Scope and Mechanistic Investigations. *Organometallics* **2018**, *37* (9), 1392−1399.
(37) Hansch, C.; Leo, A.; Taft, R. W. A Survey of Hammett Substituent Constants and Resonance and Field Parameters. *Chem. Rev.* **1991**, *91* (2), 165−195.
(38) Tsou, T. T.; Kochi, J. K. Mechanism of Oxidative Addition. Reaction of Nickel(0) Complexes with Aromatic Halides. *J. Am. Chem. Soc.* **1979**, *101* (21), 6319−6332.
(39) Shekhar, S.; Ryberg, P.; Hartwig, J. F.; Mathew, J. S.; Blackmond, D. G.; Strieter, E. R.; Buchwald, S. L. Reevaluation of the Mechanism of the Amination of Aryl Halides Catalyzed by BINAP-Ligated Palladium Complexes. *J. Am. Chem. Soc.* **2006**, *128* (11), 3584−3591.
(40) Ge, S.; Green, R. A.; Hartwig, J. F. Controlling First-Row Catalysts: Amination of Aryl and Heteroaryl Chlorides and Bromides with Primary Aliphatic Amines Catalyzed by a BINAP-Ligated Single-Component Ni(0) Complex. *J. Am. Chem. Soc.* **2014**, *136* (4), 1617−1627.
(41) Sun, R.; Qin, Y.; Nocera, D. G. General Paradigm in Photoredox Nickel-Catalyzed Cross-Coupling Allows for Light-Free Access to Reactivity. *Angew. Chem., Int. Ed.* **2020**, *59* (24), 9527−9533.
(42) Kutchukian, P. S.; Dropinski, J. F.; Dykstra, K. D.; Li, B.; DiRocco, D. A.; Streckfuss, E. C.; Campeau, L.-C.; Cernak, T.; Vachal, P.; Davies, I. W.; Krska, S. W.; Dreher, S. D. Chemistry Informer Libraries: A Chemoinformatics Enabled Approach to Evaluate and Advance Synthetic Methods. *Chem. Sci.* **2016**, *7* (4), 2604−2613.

https://dx.doi.org/10.1021/jacs.0c05901
J. Am. Chem. Soc. 2020, 142, 15830−15841

(43) Gisbertz, S.; Reischauer, S.; Pieber, B. Overcoming Limitations in Dual Photoredox/Nickel-Catalysed C–N Cross-Couplings Due to Catalyst Deactivation. *Nature Catalysis* **2020**, DOI: 10.1038/s41929-020-0473-6.

https://dx.doi.org/10.1021/jacs.0c05901
J. Am. Chem. Soc. 2020, 142, 15830–15841